*Chapter 4*

# INSTABILITY MECHANISM IDENTIFICATION: COLORIMETRIC HEIGHT RECONSTRUCTION

## 4.1 Background

In the previous chapter, the experimental data from Ref. [1] was reanalyzed to better measure the characteristic wavelength of the system. In this chapter, the same data set was used to reconstruct the height of the protrusions as a function of time. There has been previous work on a different instability driven by electric fields which examined the early time dynamics of peak growth using illumination from a laser to measure peak growth rates [37]. To date, there has been no similar study for the instability driven by large transverse thermal gradients. In this chapter, the peak elevations of the film surface are quantitatively measured *in situ* as a function of time through observation of film color, which varies due to thin-film interference effects and can remove some of the ambiguities introduced by single wavelength illumination [38]. From the peak elevations as a function of time, the growth rates of the instability peaks are measured and compared to the predictions of the TC model which was described in Ch. 2. The results presented here are consistent with general linear stability theory, and specifically support a thermocapillary mechanism for the instability. The experimental method and theoretical analysis may also be used to examine the formative dynamics of other thin-film instabilities.

## 4.2 Brief Summary of Experimental Details

The experimental setup and procedures have been described in greater detail in previous studies [1] and in Ch. 3, so this will only be a brief summary of the experimental details. A diagram of the experimental setup is shown in Fig. 4.1. The initially flat polystyrene (PS) nanofilm with thickness $h_o$ was spun coat onto a silicon wafer and placed onto a heater. The upper half of the setup was composed of a glass coverslip, a copper sheet with a hole drilled in it which supported the chiller, and a sapphire window. The sapphire window was held to the copper sheet with a vacuum and the entire top half of the setup was clamped onto the bottom half. A set of SU-8 spacers on the sapphire window prevented contact and defined the total gap spacing, $d_o$, to the bottom of the SU-8 mesa. Three different mesa thicknesses were used: 1380 nm, 1480 nm, and 0 nm (no mesa).

Figure 4.1: Diagram of the experimental setup used for optical observation

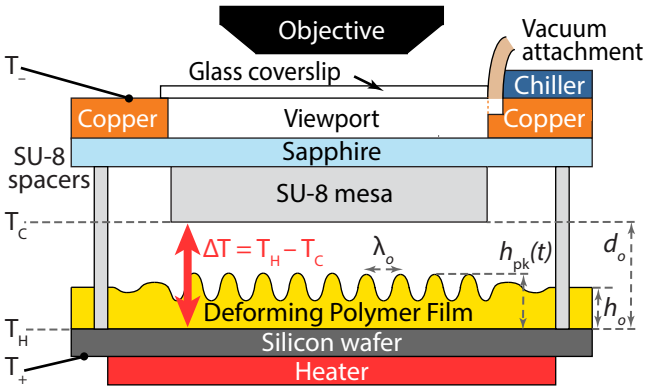


Experimental setup (not to scale). An instability in a polymer nanofilm was induced by a strong transverse thermal gradient and was observed *in situ* through a microscope objective.

Temperatures in the setup were monitored using thermocouples attached to the bottom of the silicon substrate ($T_+$) and to the top of the upper copper plate near the view port ($T_-$). Direct measurement of $T_H$ and $T_C$ (see Fig. 4.1) was not possible within the micron-scale gap due to its small dimension. Knowledge of the temperature drop $\Delta T = T_H - T_C$ is however critical for comparison to theoretical models, and therefore finite element simulations were used to compute the temperature profile of the whole setup, as described in detail in Ch. 3. The characteristic wavelength of the instability, $\lambda_o$, for these experiments has also been measured in Ch. 3 and was extracted from the peak of the power spectrum.

## 4.3 Growth Rate Predictions from Linear Stability Analysis

Previous theoretical analyses [8, 10] have shown that a long-wavelength thermocapillary instability can be generated in a nanofilm with a free interface which is subject to a large thermal gradient applied normal to the initially flat free interface. Within linear stability analysis, the instability is predicted to quickly become dominated by a maximally unstable mode of fixed wavelength in the initial linear regime. In this linear regime, the film's free interface can then be described by

$$h(x, y, t) = h_o + \delta h \; e^{bt} \; e^{i\vec{k}\cdot\vec{x}}, \tag{4.1}$$

where $\delta h$ is the initial amplitude of surface fluctuations. The wavenumber and growth rate of the maximally unstable, or fastest growing, mode were found by computing the maximum of the dispersion relation, $b(k)$, which was found by inserting Eq. (4.1) into the nonlinear differential equation describing the interface evolution [10]. The details of this derivation can be found in Ch. 2 and the dimen-

sional form of the dispersion relation is

$$b(k) = \frac{k^2}{\mu(\mathrm{T})}\left[\frac{\kappa D h_o \gamma_\mathrm{T} \Delta\mathrm{T}}{2(D+\kappa-1)^2} - \frac{\gamma h_o^3}{3}k^2\right]. \tag{4.2}$$

Based on this equation, the maximum growth rate, $b_o(k_o)$, and the corresponding maximally unstable wavevector, $k_o$, are

$$b_o = \frac{3\kappa^2\gamma_\mathrm{T}^2\Delta\mathrm{T}^2}{16\mu(\mathrm{T})h_o\gamma}\frac{D^2}{(D+\kappa-1)^4}, \tag{4.3}$$

$$k_o = \frac{2\pi}{\lambda_o} = \frac{1}{h_o}\sqrt{\frac{3\kappa\gamma_\mathrm{T}\Delta\mathrm{T}}{4\gamma}}\frac{\sqrt{D}}{D+\kappa-1}. \tag{4.4}$$

In these expressions, $\lambda_o$ is the real space wavelength, $h_o$ is the initial film thickness, $\kappa$ is the ratio of the polymer and air thermal conductivities, $\gamma_\mathrm{T}$ is the thermocapillary coefficient, $\Delta\mathrm{T}$ is the temperature drop across the polymer/air bilayer, $\gamma$ is the surface tension of the molten nanofilm, $D = d_o/h_o$ is the gap ratio, and $\mu(\mathrm{T})$ is the viscosity of the molten nanofilm at the temperature T. A summary of the definitions and ranges of values for these quantities can be found in Table 4.1. Additionally, a full listing of the experimental parameters for each run can be found in Table 4.3.

The spatial portion of Eq. (4.1) has been previously investigated using experimental measurements of $\lambda_o$ as a function of $\Delta\mathrm{T}$ and $D$ which were then compared to Eq. (4.4) [1, 39]. The temporal evolution of the film has not been studied in detail for this system. In this work, the temporal portion of Eq. (4.1)) was investigated by computing $b_o$ and comparing its functional dependence on $D$ to Eq. (4.3)). Twenty experimental runs were analyzed, and for each experimental run, the elevations of 10 peaks were tracked at intervals ranging from 10 – 120 s using white light interference colors which will be described in detail below. The temporal evolution provides a more stringent test of the linear stability predictions than spatial measurements, due to the greater powers in the experimental parameters in Eq. (4.3) as compared to Eq. (4.4). However, we also note that Eq. (4.3) and $\lambda_o$ are intimately related through the normalization

$$\beta_\Lambda \equiv b_o\frac{h_o\mu(\mathrm{T})}{\gamma_o} = \frac{(2\pi)^4}{3}\Lambda^{-4}, \tag{4.5}$$

where $\beta_\Lambda$ is a nondimensional growth rate and $\Lambda \equiv \lambda_o/h_o$ is a nondimensional wavelength. This relationship is highly general for thin film systems which have a dispersion relation of the form

$$b(k) = k^2\left(A_1 - A_2k^2\right), \tag{4.6}$$

Table 4.1: Experimental parameter ranges for the experiments where the growth rate was measured

| **Description** | **Symbol** | **Value(s)** |
|---|---|---|
| Thermal conductivity ratio | $\kappa$ | 0.242 [22, 23]] |
| PS surface tension (100 °C) | $\gamma$ | 33 mN/m [22] |
| Thermocapillary coefficient | $\gamma_T$ | 78 $\mu$N/(m–°C) [22] |
| Initial film thickness | $h_o$ | 95 – 390 nm |
| Plate separation | $d_o$ | 605 – 2200 nm |
| Gap ratio | $D$ | 1.97 – 14.1 |
| Measured wavelength | $\lambda_o$ | 29.1 – 73.2 $\mu$m [39] |
| PS-substrate interface temperature | $T_H$ | 89.8 – 101 °C [39] |
| Air-superstrate interface temperature | $T_C$ | 67.8 – 88.7 °C [39] |
| Temperature difference | $\Delta T$ | 9.83 – 25.8 °C [39] |
| Viscosity ($T_H$) | $\mu(T_H)$ | 30.9 – 94.4 Pa s [24] |
| Viscosity ($T_C$) | $\mu(T_C)$ | 104.8 – 3930 Pa s [24] |
| Measured growth rate | $b_o$ | (0.345 – 158)$\times 10^{-4}$ s$^{-1}$ |

where $A_1$ and $A_2$ are constants determined by the specific instability. Eq. (4.5) is independent of the specific instability mechanism. Thus, we first probe the general linear stability framework by comparing the data to Eq. (4.5) before comparing it to the thermocapillary model specifically.

The remainder of this chapter is organized in the following sections. First, we discuss the details of the film height and growth rate measurement process in Section 4.4. Then we compare the resulting growth rate measurements to general linear stability theory and the predictions of the thermocapillary model specifically in Section 4.5. Finally, we discuss these results and address areas which will be improved in future work.

## 4.4 Film Height and Growth Rate Measurements using Color Interferometry

In this section we describe the method used to determine the peak heights during structure formation as a function of time. Since film deformations at early times were on the scale of nanometers, care is required both to calibrate and to track evolving peak heights by white light interferometry. The general approach in this technique is to use the thin film interference equations to compute the portion of

the incident light which is reflected as a function of wavelength. This reflection spectrum is then converted to red (R), green (G), and blue (B) color values using the camera response function for each channel. These RGB triplets form a set of curves against which the experimentally measured RGB pixel can be compared. Peak locations are well-defined at late times, so the center of the peak was easily identifiable and selected for reconstruction. Then, using the fact that the film height is monotonically increasing as a function of time at the location of a peak, we worked backwards in time to find the height of the current image based on the height of the next image in time which had already been analyzed. This procedure continued until the start of the experiment and yielded the peak height as a function of time from which the growth rate was extracted using a linear fit on a semilog plot. This is similar to the technique used to measure the characteristic wavelength in Ref. [39] and was described in Ch. 3.

Peak heights as a function of time were ascertained by comparison to a color chart produced for thin-film white light interference based on transmission and reflection from the distinct material layers in the experimental setup. In this system refractive index data as a function of optical wavelength for six distinct materials was used: glass, air, sapphire, SU-8, polystyrene, and silicon. To describe the variation of the refractive index of each material as a function of wavelength, Cauchy's equation was used [40]. It describes the variation of refractive index as a function of wavelength fairly well in the visible portion of the electromagnetic spectrum for materials with normal dispersion and has the form

$$n(\lambda_{\text{opt}}) = B + \frac{C}{\lambda_{\text{opt}}^2} + \frac{D}{\lambda_{\text{opt}}^4}. \tag{4.7}$$

In this equation, $\lambda_{\text{opt}}$ is the wavelength of the optical illumination. For each material, the three constants in Eq. (4.7) can be found in Table 4.2. The refractive index of sapphire was chosen as the ordinary axis since the orientation of the window was not known and there is only one orientation where the extraordinary axis would be aligned correctly. Note that the silicon layer is the only material with significant absorption in the optical portion of the electromagnetic spectrum and so there is an additional set of Cauchy coefficients which describe the imaginary part of the refractive index as a function of wavelength. For each material, the Cauchy coefficients in Table 4.2 were substituted into Eq. (4.7) and $n(\lambda_{\text{opt}})$ was computed for 0.4 $\mu$m $\leq \lambda_{\text{opt}} \leq$ 0.8 $\mu$m in increments of 1 nm. Any refractive index values not already present in the list were linearly interpolated between the two closest values.

Table 4.2: Cauchy coefficients for the materials in the experimental setup

| Material | B | $C \times 10^2(\mu m^2)$ | $D \times 10^4(\mu m^4)$ |
|---|---|---|---|
| Polystyrene [41] | 1.563 | 0.929 | 1.20 |
| SU-8 [32] | 1.566 | 0.796 | 1.40 |
| Sapphire [42] | 1.750 | 0.654 | -1.31 |
| Corning 1737 [29] | 1.505 | 0.455 | -0.218 |
| Silicon (real) [43] | 3.819 | -17.2 | 727 |
| Silicon (imag.) [43] | 0.106 | -8.14 | 167 |

The reflectance of the experimental setup was calculated using a matrix formulation detailed in Ref. [44]. Within this formalism, both the transmission across an interface and the propagation through a homogeneous layer are represented by 2×2 matrices, which are then multiplied together for each layer in the stack to yield a single matrix. The reflectance can then be extracted easily from the elements of the total transfer matrix.

Assuming normal incidence of illumination from above through the microscope objective, the illumination beam undergoes reflection and transmission through a stack of $N-1$ internal interfaces separating $N$ uniform planar interfaces comprising linear, isotropic, and homogeneous media. The index $j = 1$ denotes the first layer, which in this study is the glass coverslip. The index $j = N$ is the last layer, which in this study is silicon. The system is assumed to be bounded by two semi-infinite air layers corresponding to $j = 0$ and $j = N + 1$. The Fresnel amplitude reflection and transmission coefficients corresponding to the interface separating layers $j$ and $j + 1$ are given by [45]

$$r_{j,j+1} = \frac{n_j - n_{j+1}}{n_j + n_{j+1}}, \tag{4.8}$$

$$t_{j,j+1} = \frac{2n_j}{n_j + n_{j+1}}. \tag{4.9}$$

The matrix describing transmission across an interface from layer $j$ to layer $j + 1$ is given by [44]

$$\mathbf{M}_{j,j+1} = \frac{1}{t_{j,j+1}} \begin{bmatrix} 1 & r_{j,j+1} \\ r_{j,j+1} & 1 \end{bmatrix}. \tag{4.10}$$

Similarly, the matrix describing propagation through a layer $j$ is given by [44]

$$\mathbf{M}_j = \begin{bmatrix} e^{-i\delta_j} & 0 \\ 0 & e^{-i\delta_j} \end{bmatrix}. \tag{4.11}$$

In this expression the phase accumulated by passing through a layer is denoted by $\delta_j$ and has the form

$$\delta_j(\lambda_{\text{opt}}) = \frac{2\pi n_j}{\lambda_{\text{opt}}} z_j, \tag{4.12}$$

where $\lambda_{\text{opt}}$ denotes the optical wavelength and $z_j$ is the thickness of layer $j$. To construct the total transfer matrix through the multilayer stack, we simply multiply the matrices together to yield

$$\mathbf{M} = \mathbf{M}_{0,1}\mathbf{M}_1\mathbf{M}_{1,2}\mathbf{M}_2 \ldots \mathbf{M}_N\mathbf{M}_{N,N+1} = \begin{bmatrix} M_{1,1} & M_{1,2} \\ M_{2,1} & M_{2,2} \end{bmatrix}. \tag{4.13}$$

Recall that the entire stack is assumed to be bounded on both sides by semi-infinite air layers so that layer $j = 0$ and $j = N + 1$ are simply air with a refractive index of 1. It can be shown [44] that the total reflectance of the multilayer stack is then

$$R(\lambda_{\text{opt}}, h) = \frac{|M_{2,1}|^2}{|M_{1,1}|^2}. \tag{4.14}$$

Due to the dependence of $\delta_j$ and $n_j$ on the optical wavelength, $\lambda_{\text{opt}}$, the reflectance also is wavelength dependent. Furthermore, the reflectance depends on the thickness of the polymer nanofilm, $h$, implicitly through $\delta_j$ and we have explicitly highlighted this dependence in Eq. (4.14).

Fringe color values can therefore be computed as a function of $h$ by estimating the convolution integral for each color channel $\alpha$, where $\alpha = 1 \rightarrow$ red, $\alpha = 2 \rightarrow$ green, and $\alpha = 3 \rightarrow$ blue

$$\mathrm{v}_{\text{theor}}(h, \alpha) = \int I(\lambda_{\text{opt}})\, R(\lambda_{\text{opt}}, h)\, S_\alpha(\lambda_{\text{opt}})\, d\lambda_{\text{opt}}. \tag{4.15}$$

Here, $I(\lambda_{\text{opt}})$ represents the spectrum of the halogen light source (Osram HLX 64625, 12 V, 100 W max) as measured with a spectrometer (USB4000-VIS-NIR,

Figure 4.2: Theoretical interference fringe color for films with different thicknesses

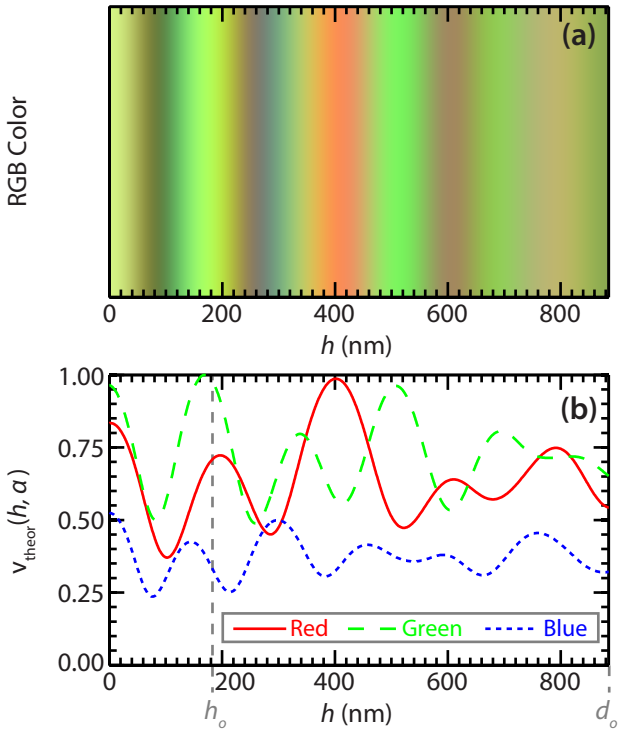


Sample plots of theoretical interference fringe color $\mathrm{v}_{\mathrm{theor}}(h, \alpha)$ as a function of PS film thickness, $h$, as predicted by Eq. (4.15) for experiment number #56. (a) Interference spectrum as a function of film thickness expressed as RGB triplets. (b) Interference spectrum as a function of film thickness expressed numerically.

Ocean Optics) at the exit of the microscope objective. $S_\alpha(\lambda_{\mathrm{opt}})$ denotes the spectral responsivity of the camera (DVC 1312C) for a given channel $\alpha$ as provided by the manufacturer. An example of computed values for $\mathrm{v}_{\mathrm{theor}}(h, \alpha)$ versus the film thickness $h$ is shown in Fig. 4.2 for $d_{\mathrm{o}}$ = 885 nm and SU-8 mesa thickness = 1380 nm in experimental run #56. Note that these curves have been normalized so that the maximum value among all the channels is equal to 1 and that the numbering convention is consistent with Refs. [39] and Ch. 3.

The curves shown in Fig. 4.2 represent what we would expect to see with the camera in the experimental setup. However, they fail to account for the experimental brightness and white balance settings. The experimental brightness determines the amplitude of the curves from Fig. 4.2 based on the exposure time of the camera. The camera will also adjust the relative weight of each channel to achieve white balance under a given set of illumination conditions. To compensate for these effects, each theoretical curve was independently normalized by a linear scaling which spanned the minimum and maximum values of the experimentally measured values. This

transformation from $\mathrm{v}_{\mathrm{theor}}(h,\alpha)$ to $\tilde{\mathrm{v}}_{\mathrm{theor}}(h,\alpha)$, which helped account for differences introduced by experimental brightness and white balance conditions, was performed according to Eq. (4.16)

$$\begin{aligned} \min_{h\in[h_o,h_f]} \tilde{\mathrm{v}}_{\mathrm{theor}}(h,\alpha) &= \min_{t\in[0,t_f]} \mathrm{v}_{\mathrm{exp}}(x_f,y_f,t,\alpha), \\ \max_{h\in[h_o,h_f]} \tilde{\mathrm{v}}_{\mathrm{theor}}(h,\alpha) &= \max_{t\in[0,t_f]} \mathrm{v}_{\mathrm{exp}}(x_f,y_f,t,\alpha). \end{aligned} \tag{4.16}$$

In these equations $x_f$ and $y_f$ are the location of the peak at the time of the final image, $t_f$. The final height $h_f$ is the estimated height of the peak at $t_f$. In most cases this equals $d_o$ because the peak touched the SU-8 mesa. In some cases, particularly when there was no mesa, the peaks did not touch the upper plate and so the final height was not equal to $d_o$. In these cases $h_f$ was estimated by matching the experimental peak color to the theoretical interference colors by hand.

Measurements of the peak amplitudes during film growth, $h_{\mathrm{pk}}(t)$, were then estimated as follows. A cost function was defined in order to minimize differences between the experimental RGB values as a function of time and the theoretical color variations expected as a function of the local film thickness according to

$$g(x,y,t,h) = \sum_{\alpha=1}^{3} \left[ \left( \mathrm{v}_{\mathrm{exp}}(x,y,t,\alpha) - \tilde{\mathrm{v}}_{\mathrm{theor}}(h,\alpha) \right) \right]^2 . \tag{4.17}$$

Because the color of the film oscillates in $h$, finding the global minimum of this cost function does not accurately provide the film thickness at an arbitrary time due to noise and uncertainties in the thicknesses of the layers in the system. We worked backwards frame-by-frame, starting with the estimated height of the final frame where the peak was easily identified. We then restricted the range of $h$ within which we searched for a minimum of $g$ to a 70 nm window in height below the most recently computed height since the peak heights increase monotonically. Additionally, we allowed the location of the peak $(x_{\mathrm{pk}}(t),\ y_{\mathrm{pk}}(t))$ to shift by one pixel in the $x$-direction or one pixel in the $y$-direction between frames, and hence computed the film elevation for the five pixels within a 1-pixel radius neighborhood of the peak from the previously analyzed frame. This allows for a small amount of lateral movement in the peak location during each time step, $\Delta t$. The measured height $h_{\mathrm{meas}}(x,y,t)$ of each pixel within this neighborhood at time $t$ was given by the value of $h$ that minimizes $g(x,y,t,h)$ subject to the constraint, $h \in \left[ h_{\mathrm{pk}}(t+\Delta t) - 70\ \mathrm{nm},\ \ h_{\mathrm{pk}}(t+\Delta t) \right]$. $h_{\mathrm{pk}}(t)$

and $(x_{\rm pk}(t),\ y_{\rm pk}(t))$ are then given by the value and location of the largest $h_{\rm meas}(x, y, t)$ within the neighborhood at time $t$.

A typical sequence of peak growth images is displayed in Fig. 4.3, showing only three of the ten peaks tracked in this sample. Each of the three analyzed peaks is highlighted by a circle in Fig. 4.3(b), (c), and (d). Once a peak was selected, the RGB pixel values of the peak center at $(x_f, y_f)$ were extracted as a function of time and these values are plotted in Fig. 4.4(b) for the uppermost peak in Fig. 4.3. From the maximum and minimum values for each channel, the theoretical interference spectrum curves from Fig. 4.2 were scaled to produce the $\tilde{\rm v}_{\rm theor}(h, \alpha)$ curves for this experiment which are shown in Fig. 4.4(c). Note that as compared to the unscaled $\rm v_{theor}(h, \alpha)$ in Fig. 4.2, these colors match the experimental images much more accurately. Then, each vertical time slice in Fig. 4.4(b) was used to define an RGB triplet which was compared against the curve in Fig. 4.4(c), restricted to be within 70 nm of the most recently reconstructed height, and the cost function was minimized to yield the reconstructed height. Generally, these fits are fairly robust, particularly at height values less than $1.5h_o$. However, when the $\tilde{\rm v}_{\rm theor}(h, \alpha)$ curves are flat the reconstructed height can jump with small discontinuities. This is evident in Fig. 4.4(c) near $h$ = 500 nm and $h$ = 750 nm where two channels have extrema simultaneously. After this step, the reconstructed heights are plotted as a function of time in Fig. 4.4(d). At very early times (0 – 100 min in Fig. 4.4), fluctuations in film elevation are too small (< 20 nm) to be reliably measured *in situ*. After this point a linear growth regime consistent with the form of Eq. (4.1) is observed, and the growth rate $b_{\rm max}$ is recorded from the linear fit to the semilogarithmic data. For each experiment, the data was fit to the heights which satisfied 20 nm $\leq h_{\rm pk} - h_o \leq h_o/2$. The lower bound was chosen due to limitations in our measurement technique where the height data became very noisy. The upper bound was chosen to avoid the regime where nonlinear factors become dominant, such as contact with the top plate (e.g., the middle peak in Fig. 4.3) or local film depletion. This work only investigates the linear portion of the growth to compare to the predictions of linear stability analysis. A full listing of all the measured growth rate values can be found in Table 4.4.

## 4.5 Comparison of Observed Growth Rate to Linear Stability Analysis Predictions

With the measured growth rates, $b_o$, we investigated the predictions of general linear stability theory and then the specific predictions of the thermocapillary model. We first used the measured growth rates to validate general linear stability theory by

Figure 4.3: Images of peak growth as a function of time

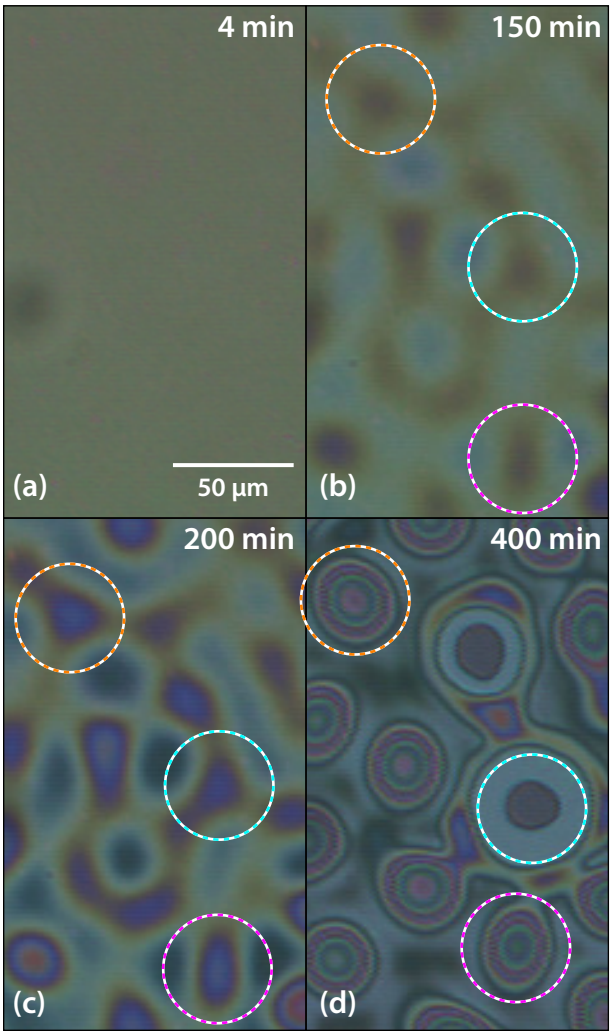


Brightfield micrographs showing thin-film interference colors in the destabilizing film under 10x magnification for experiment number #56. (a) At very early times, the film is flat and no peaks are visible. (b) Peaks begin to grow and can be identified as regions of darker color in this image. Three of the analyzed peaks are circled. (c) Peaks continue to grow and become more distinct. (d) At late times, the peaks are quite tall and show interference fringes (top and bottom) or have contacted the SU-8 mesa (middle).

Figure 4.4: Analysis of peak growth as a function of time and example of growth rate measurement

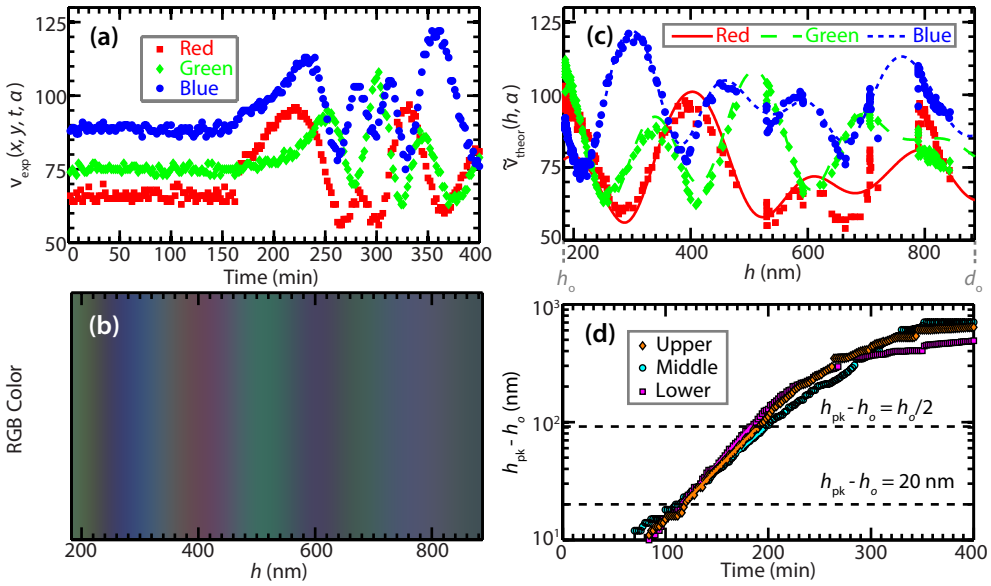


Typical growth rate measurements. (a) Experimental RGB pixel values, $v_{exp}(x, y, t, \alpha)$, as a function of time for the uppermost encircled peak from (a). (b) Scaled interference spectrum as a function of film thickness. (c) Scaled interference spectrum data for this experimental run which will be used to compute the cost function, $g(x, y, t, h)$. The matched $v_{exp}$ points for the upper peak are also plotted to show the matching. (d) Peak elevations deduced from the interference colors matched from (c) for each of the three circled peaks in Fig. 4.3. Lines are fitted to the growth regime 20 nm $\leq h_{pk} - h_o \leq h_o/2$ in order to determine $b_o$.

examining their relationship to the characteristic wavelength $\lambda_o$ which was shown in Eq. (4.5). The details of the $\lambda_o$ measurements for these experiments have been described previously in Ref. [39] and Ch. 3.

When comparing to linear stability theory, the temperature at which to evaluate the viscosity is not entirely clear. In the theoretical analysis of Dietzel and Troian [8, 10] the viscosity was assumed to be constant and equal to the value of the viscosity at the temperature of the PS-substrate interface ($T_H$ in Table 4.1) to complete the nondimensionalization of the Navier-Stokes equations. However, the viscosity of PS varies significantly with temperature and due to the large thermal gradient applied across the system there was a range of potential viscosities. The viscosity values for the PS have been linearly interpolated in temperature from a series of measurements made by Urakawa *et al.* [24] over a temperature range of 62 °C to 216 °C. They used PS from the same manufacturer (Scientific Polymer Products) with a slightly higher molecular weight ($M_w$ = 1.9 kg/mol vs. $M_w$ = 1.3 kg/mol in this study), but their results for the glass transition temperature agree with our experimental

Figure 4.5: Nondimensional growth rate plotted as a function of nondimensional wavelength

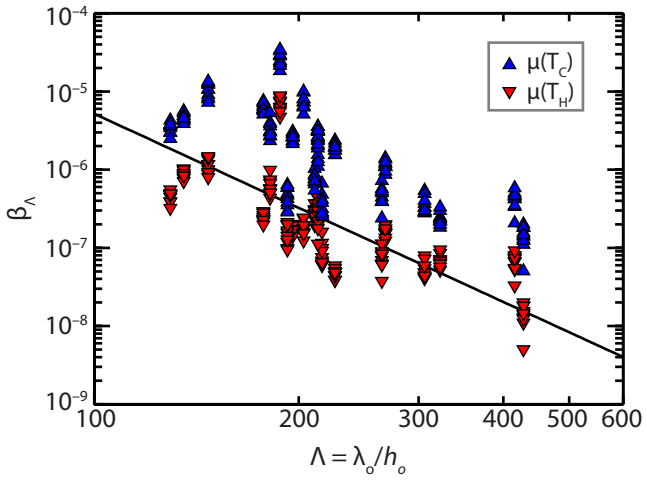


Black line: prediction given by Eq. (4.5). Red triangles: Nondimensional growth rates computed from $b_o h_o \mu(\mathrm{T_H})/\gamma$. Blue triangles: Nondimensional growth rates computed from $b_o h_o \mu(\mathrm{T_C})/\gamma$.

observations where $\mathrm{T}_g$ is approximately 60 °C. Comparing the viscosity of PS at the temperature of the PS-substrate interface ($\mathrm{T_H}$) and the air-superstrate interface ($\mathrm{T_C}$) shows a difference of up to two orders of magnitude (see $\mu(\mathrm{T_H})$ and $\mu(\mathrm{T_C})$ in Table 4.1). The experimental viscosity should be larger than $\mu(\mathrm{T_H})$ and smaller than $\mu(\mathrm{T_C})$ because viscosity is a monotonically decreasing function of temperature. Since it should lie between these two bounding values we can probe the consistency of Eq. (4.5) by using them as lower and upper bounds when nondimensionalizing $b_o$.

As seen in Fig. 4.5, the points (red triangles) where the growth rate measurements, $b_o$, were normalized by $\mu(\mathrm{T_H})$ almost all lie beneath the solid black line which corresponds to Eq. (4.5). Similarly, the points (blue triangles) which normalized the growth rate by $\mu(\mathrm{T_C})$ almost all lie above the solid black line. This bracketing shows the consistency of our data with the general expression given above. For the remainder of this paper, we will use the viscosity computed from the temperature at the initially flat PS-air interface ($\mathrm{T_{Int}}$).

To test the predictions of the thermocapillary theory specifically, the dependence of the growth rate on the gap ratio $D \equiv d_o/h_o$ was examined. Our previous thermocapillary wavelength analysis on this experimental data in Ch. 3 had determined that this experimental data is best described by a constant $C_{\mathrm{TC}} = 2\pi\sqrt{(4\gamma)/(3\kappa\gamma_T)}) = 447\ (^\circ\mathrm{C})^{1/2}$ which encapsulates all the material parameters of the system [39]. The

Figure 4.6: Nondimensional growth rates plotted as functions of normalized gap ratio

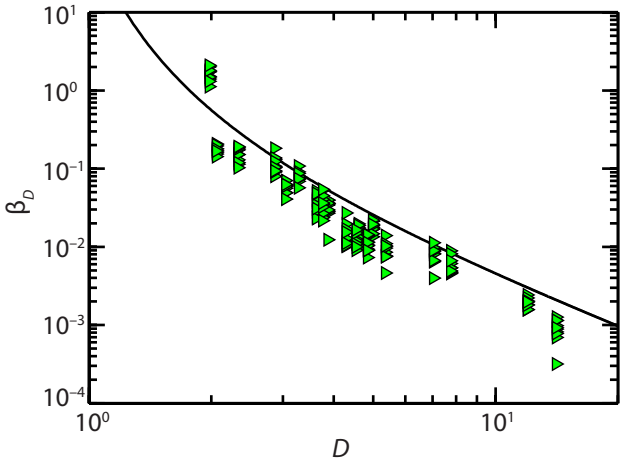


The solid black curve is given by Eq. (4.18) and the data points are the measured growth rates normalized to isolate the functional dependence on $D$.

use of this constant compensates for the fact that some of the values listed in Table 4.1 had to be extrapolated in molecular weight or were not provided with any molecular weight data. Since it was derived from a fit of experimental wavelength measurements to this same data set it is a more reliable quantity to make comparisons with. To ensure consistency between the wavelength analysis [39] and the current growth rate analysis, this value was held fixed. The functional dependency of $b_o$ on $D$ can be isolated by new scalings of the growth rate using the constant $C_{\mathrm{TC}}$ with Eq. (4.3)

$$\beta_D \equiv b_o \frac{\mu(\mathrm{T_{Int}}) h_o (2\pi)^4}{\gamma_o (\Delta \mathrm{T})^2 (C_{\mathrm{TC}})^4} = \frac{D^2}{3\,(D+\kappa-1)^4}. \tag{4.18}$$

The dependence of $\beta_D$ on $D$ is plotted in Fig. 4.6. As in Fig. 4.5, the measured growth rate is slightly smaller than expected with the data below the solid black curve. Recall from Ch. 2 that the TC model was derived under the assumption of constant viscosity, whereas in experiment the viscosity changes as the film deforms. Nevertheless, the agreement is remarkably good. This data lends further support to the thermocapillary theory, although it should be noted that this data barely spans a decade in $D$ so more data is necessary to confirm these results.

## 4.6 Discussion of Results

To this point, the experimental data suggests that the thermocapillary mechanism is the dominant cause of this instability. However, there are several areas where these experiments could be improved. First, it was determined after the completion of these experiments that the sapphire windows that were used had a random crystallographic orientation. Sapphire is birefringent which means that the refractive index depends on the orientation of the crystal. If the c-axis of the sapphire is not parallel to the optical axis, then the value for the refractive index used above will not accurately capture the phase delay in the sapphire in the calculation of the interference colors. This in turn could affect the reconstructed height values. We expect this effect to be small, but this issue has been rectified in the redesigned experimental setup which is presented in Ch. 5. Additionally, we wanted to probe the functional dependence of $b_o$ on $\Delta$T as well as $D$ but these experiments did not span a suitably large range of $\Delta$T, only 10 – 26 °C, to permit a meaningful comparison to the theoretical predictions.

## 4.7 Summary

In this chapter we analyzed the early time growth dynamics of a molten nanofilm exposed to a destabilizing transverse thermal gradient. By using differential colorimetry to match the color of a deforming nanofilm to a height value we reconstructed the height of the peaks as a function of time. From this, the growth rate was measured during the linear regime. We have found that linear stability theory describes the growth rate of peaks in the unstable film by investigating the dependence of the nondimensional growth rate on the nondimensional wavelength. Furthermore, we found that the thermocapillary mechanism is consistent with the measured linear growth rates of the instability as a function of gap ratio, $D$. These results lend further credence to the thermocapillary mechanism and show avenues for experimental improvements in future nanofilm experiments.

Table 4.3: Growth rate analysis parameters and derived values

| Exp. No. | $d_o$ (nm) | $h_o$ (nm) | $D$ | SU-8 disk thickness ($\mu$m) | $\lambda_o$ ($\mu$m) | $T_H$ (°C) | $T_{Int}$ (°C) | $T_C$ (°C) | $\Delta T$ (°C) | $\eta(T_H)$ (Pa s) | $\eta(T_{Int})$ (Pa s) | $\eta(T_C)$ (Pa s) | Min $b_o$ $\times 10^{-4}$ (1/s) | Max $b_o$ $\times 10^{-4}$ (1/s) | Avg. $b_o$ $\times 10^{-4}$ (1/s) |
|---|---|---|---|---|---|---|---|---|---|---|---|---|---|---|---|
| 46 | 900 | 189 | 4.76 | 1.38 | 37.0 | 93.6 | 92.4 | 73.8 | 19.8 | 60.6 | 70.4 | 925 | 4.11 | 5.89 | 5.03 |
| 47 | 810 | 189 | 4.29 | 1.38 | 40.9 | 99.0 | 98.1 | 86.3 | 12.7 | 36.1 | 38.5 | 152 | 2.94 | 7.79 | 4.18 |
| 48 | 840 | 183 | 4.59 | 1.38 | 32.5 | 89.9 | 88.6 | 69.3 | 20.6 | 93.9 | 105 | 2440 | 3.84 | 5.68 | 4.78 |
| 50 | 900 | 181 | 4.97 | 1.38 | 48.5 | 96.8 | 95.8 | 80.8 | 16.0 | 45.2 | 49.6 | 323 | 4.99 | 8.13 | 6.57 |
| 51 | 700 | 181 | 3.87 | 1.48 | 38.6 | 91.8 | 90.5 | 75.4 | 16.4 | 76.5 | 87.9 | 755 | 2.70 | 8.74 | 7.01 |
| 52 | 605 | 185 | 3.27 | 1.48 | 39.1 | 98.5 | 97.6 | 88.7 | 9.83 | 37.2 | 41.2 | 105 | 9.45 | 17.9 | 13.1 |
| 53 | 830 | 183 | 4.54 | 1.38 | 59.1 | 100 | 99.7 | 88.1 | 12.4 | 33.0 | 34.6 | 116 | 2.87 | 5.23 | 3.79 |
| 54 | 670 | 185 | 3.62 | 1.48 | 35.6 | 99.0 | 98.1 | 88.4 | 10.6 | 36.2 | 38.7 | 109 | 4.73 | 10.7 | 7.53 |
| 56 | 885 | 183 | 4.84 | 1.38 | 37.2 | 89.8 | 88.6 | 67.8 | 22.1 | 94.4 | 106 | 3930 | 2.39 | 4.68 | 3.50 |
| 58 | 760 | 142 | 5.35 | 1.48 | 37.6 | 96.1 | 95.3 | 81.1 | 15.0 | 48.3 | 52.1 | 310 | 1.83 | 5.51 | 3.60 |
| 60 | 735 | 95.0 | 7.74 | 1.48 | 29.1 | 95.9 | 95.4 | 80.4 | 15.5 | 49.3 | 51.8 | 337 | 2.91 | 5.65 | 3.79 |
| 61 | 710 | 101 | 7.03 | 1.48 | 42.0 | 95.8 | 95.2 | 80.9 | 14.9 | 50.0 | 52.8 | 319 | 2.16 | 6.10 | 4.41 |
| 62 | 785 | 258 | 3.04 | 1.48 | 33.4 | 93.9 | 92.2 | 78.2 | 15.7 | 59.3 | 72.2 | 461 | 7.03 | 12.1 | 9.83 |
| 63 | 754 | 201 | 3.75 | 1.48 | 42.9 | 94.1 | 92.9 | 78.7 | 15.5 | 58.0 | 66.3 | 413 | 5.09 | 12.8 | 8.65 |
| 64 | 615 | 215 | 2.86 | 1.48 | 39.0 | 93.1 | 91.6 | 80.1 | 13.0 | 64.6 | 78.1 | 351 | 10.4 | 23.8 | 15.1 |
| 66 | 2200 | 156 | 14.1 | 0 | 66.8 | 101 | 101 | 81.0 | 20.3 | 30.9 | 31.7 | 314 | 0.345 | 1.38 | 0.974 |
| 69 | 2200 | 184 | 12.0 | 0 | 41.6 | 97.2 | 96.6 | 71.4 | 25.8 | 43.2 | 45.9 | 1740 | 1.62 | 2.49 | 1.99 |
| 71 | 850 | 366 | 2.32 | 1.48 | 53.8 | 93.7 | 91.3 | 77.4 | 16.4 | 59.9 | 81.3 | 549 | 12.1 | 22.5 | 17.7 |
| 72 | 680 | 331 | 2.05 | 1.48 | 44.8 | 93.0 | 90.6 | 79.9 | 13.1 | 65.6 | 87.6 | 359 | 10.9 | 15.9 | 13.5 |
| 74 | 770 | 390 | 1.97 | 1.48 | 73.2 | 96.2 | 94.0 | 84.7 | 11.5 | 47.9 | 58.9 | 187 | 84.5 | 158 | 122 |

Listing of all experiments analyzed along with relevant parameter values: $d_o$ is the separation distance between the hot and cold plates; $h_o$ is the initial thickness of the PS nanofilm; $D$ is the normalized separation distance; SU-8 disk thickness denotes the overall separation distance between the hot silicon wafer and the cold sapphire window minus $d_o$; $\lambda_o$ is the measured instability wavelengths from Ref. [39]; $T_H$ and $T_C$ are the temperatures at the hot and cold plates, respectively; $\Delta T$ is the difference between $T_H$ and $T_C$ and all temperature values were taken from the simulations in Ref. [39]; $\mu(T_H)$ and $\mu(T_C)$ are the viscosity values computed at the temperatures of the hot and cold substrates, respectively; the last three columns show the minimum, maximum, and mean values of the measured growth rate, $b_o$.

Table 4.4: Measured growth rates for each experimental run reported in units of $10^{-4}$ 1/s

| 46 | 47 | 48 | 50 | 51 | 52 | 53 | 54 | 56 | 58 | 60 | 61 | 62 | 63 | 64 | 66 | 69 | 71 | 72 | 74 |
|---|---|---|---|---|---|---|---|---|---|---|---|---|---|---|---|---|---|---|---|
| 5.89 | 5.63 | 4.22 | 6.54 | 5.94 | 17.9 | 3.46 | 4.91 | 3.46 | 5.51 | 5.65 | 5.02 | 10.3 | 8.14 | 14.0 | 1.38 | 2.49 | 20.5 | 13.0 | 106 |
| 5.18 | 2.94 | 5.39 | 6.26 | 2.70 | 13.3 | 3.56 | 7.77 | 4.57 | 3.03 | 2.91 | 2.16 | 9.68 | 9.50 | 10.4 | 0.756 | 2.29 | 17.9 | 15.9 | 114 |
| 4.43 | 3.33 | 5.04 | 7.85 | 6.21 | 11.4 | 3.76 | 8.24 | 2.39 | 4.36 | 3.00 | 3.51 | 8.49 | 12.4 | 13.5 | 0.888 | 1.87 | 15.3 | 15.0 | 131 |
| 5.53 | 4.84 | 5.68 | 6.23 | 7.95 | 12.2 | 2.87 | 7.08 | 3.06 | 3.38 | 5.17 | 4.45 | 8.45 | 5.56 | 23.8 | 1.24 | 2.09 | 17.8 | 12.3 | 131 |
| 5.65 | 2.99 | 4.50 | 8.13 | 8.69 | 15.1 | 3.94 | 10.7 | 3.76 | 3.00 | 3.45 | 4.38 | 12.1 | 6.31 | 17.2 | 1.07 | 1.62 | 13.4 | 13.9 | 84.5 |
| 5.03 | 3.69 | 4.53 | 4.99 | 7.84 | 13.2 | 3.75 | 5.86 | 3.39 | 4.05 | 3.03 | 4.74 | 10.5 | 7.59 | 17.9 | 0.962 | 1.63 | 14.1 | 15.5 | 151 |
| 4.48 | 7.79 | 4.79 | 6.29 | 7.56 | 12.2 | 4.73 | 9.75 | 4.68 | 3.82 | 3.88 | 5.28 | 10.8 | 10.6 | 16.1 | 0.848 | 2.03 | 21.0 | 11.8 | 112 |
| 4.11 | 2.99 | 5.46 | 6.89 | 6.52 | 14.4 | 3.45 | 9.96 | 2.96 | 1.83 | 3.42 | 3.63 | 10.2 | 12.8 | 11.9 | 1.25 | 1.85 | 21.9 | 13.7 | 136 |
| 5.03 | 4.43 | 4.39 | 5.45 | 8.74 | 12.3 | 5.23 | 4.73 | 3.73 | 2.96 | 3.14 | 4.86 | 7.03 | 5.09 | 13.6 | 0.345 | 2.03 | 12.1 | 10.9 | 158 |
| 4.97 | 3.19 | 3.84 | 7.17 | 7.94 | 9.45 | 3.15 | 6.35 | 2.95 | 4.07 | 4.23 | 6.10 | 10.8 | 8.55 | 12.2 | 1.00 | 2.03 | 22.5 | 12.9 | 99.0 |

Listing of all experimental runs with the ten measured growth rates. The top row of the table contains the experiment number, consistent with Table 4.3. The next ten rows are the measured growth rates.